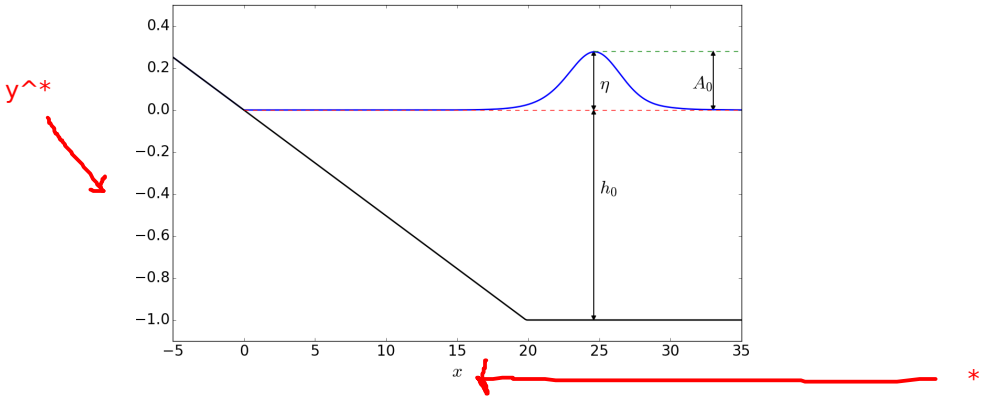

Figure 5: Definition sketch for shoaling and runup of solitary waves. The scale on the axes is the equilibrium depth, h_0.

Moreover, the measurements showed that the boundary layer flow during run-up was mostly laminar, albeit indications of transition was observed in the upper part of the swash tongue close to flow reversal. Hence, it is not appropriate to employ a Manning friction term and we compare the models without any bed friction, while leaving the experiments out.

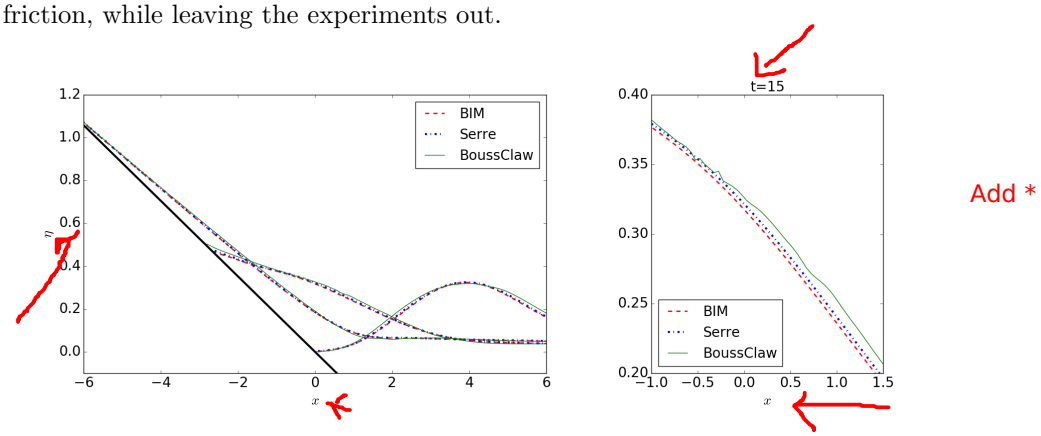

Figure 6: Runup of non-breaking solitary wave ($\alpha = 0.3$ and $\theta = 10°$). Left panel displays surfaces from the BIM, Serre and BoussClaw models at $t^* = 10, 15, 20$ for $\Delta x^* = 0.05$. Right figure is a zoom of the results at $t^* = 15$

In Figure 6, the numerical results from BIM, Serre, and BoussClaw are shown at $t^* = 10$, 15, and 20, and a zoom at $t^* = 15$ is shown on the right.

Model	BIM	Serre	BoussClaw	NLSW
Max. Run-up/Amp.	4.2432	4.2488	4.0941	4.6561

Table 1: Maximum run-up height divided by the incoming wave amplitude (R^*/α) for $\alpha = 0.3$ and $\theta = 10°$.

for comparison with the BoussClaw model. Experimental date is obtained at Synolakis et al. (2008).

In Figure 9, the laboratory measurements are shown with the computational results from the BoussClaw (in Boussinesq and NLSW mode), the Serre and the BIM models for $\alpha = 0.28$ and a $1 : 19.85$ slope at $t^* = 15$. The grid size Δx^* is 0.05 in the following simulations unless stated otherwise. This is before the wave breaks and the BoussClaw , the Serre, and the BIM model are all in good agreement with the experiments.

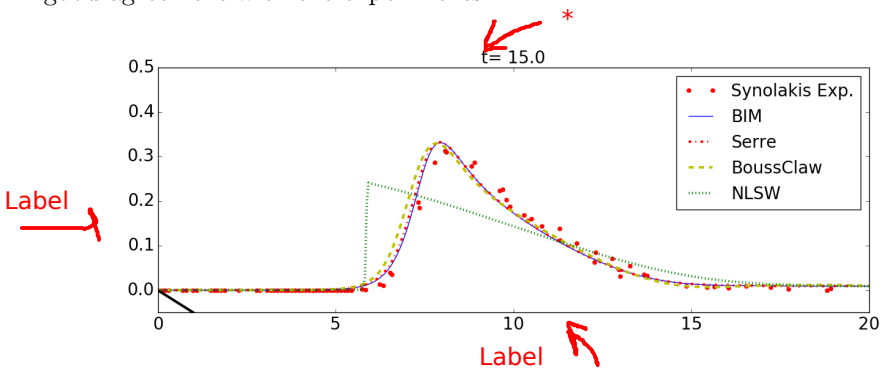

Figure 9: The surface elevation, η^* as function of x^* at $t^* = 15$ from the laboratory experiments (Synolakis, 1987) ($\alpha = 0.28$, slope $1 : 19.85$), the BIM, the Serre, the BoussClaw and the NLSW models.

The ratio of amplitude to depth, A^*/h^* (A^* is the maximum value of η^* and h^* is the equilibrium depth at the corresponding location), is about 2 at the point of breaking. The potential flow model cannot be run much beyond the breaking points (until the attachment of the plunger only) and gives no information on the following bore propagation. In figure 10 we have compared the experimental data with the BoussClaw model of $C_d^* = 0$ and 0.03.

The agreement is good and the introduction of bed-friction even seem to

match the truncated swash tongue of the experiments well. However, this may be a coincidence. Even though the wave has broken and some irregular flow features are introduced thereby, we have no evidence of the flow state being anywhere near turbulent, which is required for a quadratic bottom resistance to be appropriate. Capillary effects and experimental errors may also affect the comparison as observed by Pedersen et al. (2013).

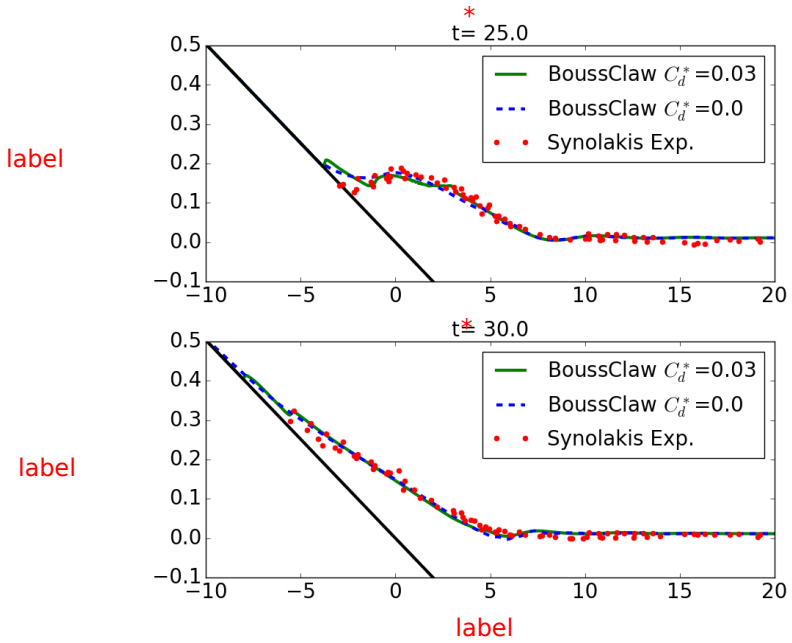

Figure 10: The surface elevation η^* as function of x^* at $t^* = 25, 30$ for the breaking case ($\alpha = 0.28$ and a $1 : 19.85$ slope). Experiments and BoussClaw results with and without bottom drag are included. The resolution in the model is $\Delta x^* = 0.05$.

In Figure 11 and Table 2, we show the run-up height in time and the maximum run-up height respectively. Unlike what was observed for $\theta = 10°$, the NLSW model reduces the run up height. The opposite behavior for the two may be explained by two competing effects of dispersion. First, for a non-breaking wave the omission of non-hydrostatic effects lead to an excessive steepening of the wave front which implies higher run-up. On the other hand, the premature breaking dissipates energy and will reduce run-up heights. For the steeper slope, there is insufficient time for the second effect to fully counterbalance the first.

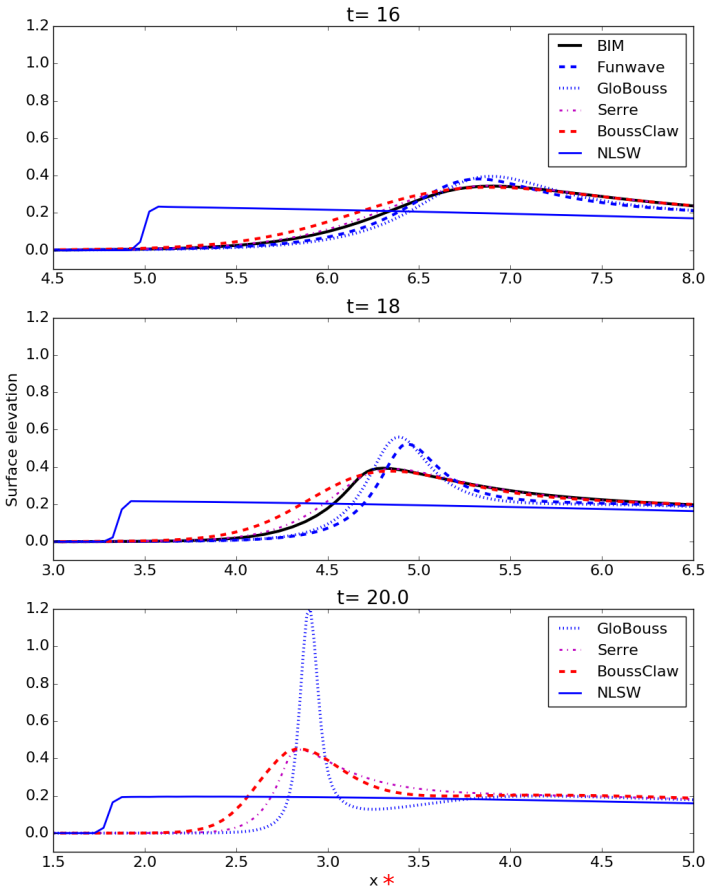

Stars

Maybe eta^* instead of text on abcissa.

Figure 12: Evolution of η^* for $\alpha = 0.28$ and a $1 : 19.85$ slope. Surfaces from the BIM, Serre, GloBouss, BoussClaw and Funwave models at $t^* = 16,\ 18,\ 20$ are included. The BoussClaw model is used with B=1/15, and the Peregrine's equations are used for GloBouss.

365 and the difference from the BoussClaw result becomes larger at $t^* = 20$. At the $t^* = 20$ there are no results from the BIM model as the wave has broken. Our observations are in line with those of Wei et al. (1995b).

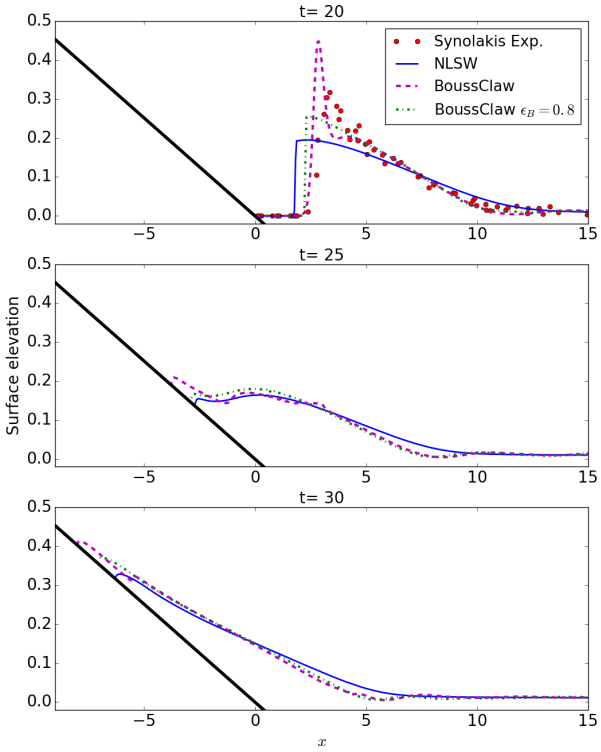

Stars.

Figure 13: Breaking case ($\alpha = 0.28$ and a $1 : 19.85$ slope). Comparison of η^* from BoussClaw and NLSW with $\epsilon_B = 0.8$ and $\Delta x^* = 0.05$ at $t^* = 20$, 25 and 30. Friction forces have been added with $C_d^* = 0.03$ in all simulations.

x_c^*. In the left panel we observe that the E_0^* is nearly constant for the shallow water equations until a shock is formed around $x_c^* = 13$. Thereafter, energy is quickly dissipated. For the BoussClaw simulations E_0^* increases slightly, but noticeably, during shoaling, indicating that E_1^* needs to be accounted for. In the BoussClaw simulation with no threshold (right panel) $E_0^* + E_1^*$ is nearly constant when the wave propagates in constant depth. On the deeper parts of the slope there is first a small increase, then a very moderate reduction. Presumably, the increase is due to the absence of strict energy conservation

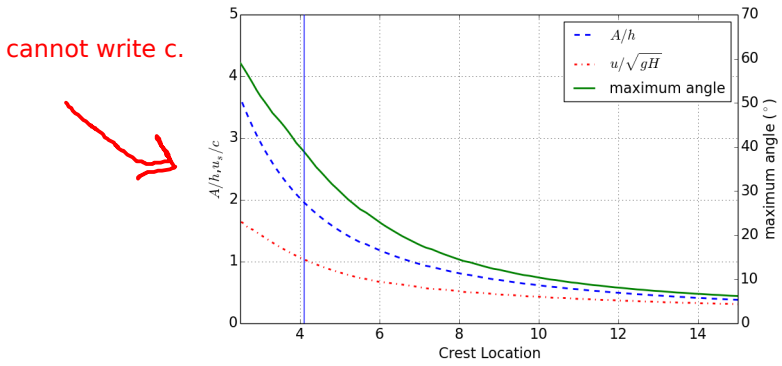

Figure 14: Plot of A^*/h^*, $u^*/\sqrt{H^*}$ and maximum angle of waves vs. crest location. The vertical line indicates where the BIM model yields breaking ($x^* = 4.09$).

in the Boussinesq equations. Close to the shoreline this tiny increase is then dominated by a stronger, but still mild, energy dissipation. When the threshold $\epsilon_B = 0.8$ is invoked there is no difference from the full Boussinesq solution until the threshold is reached for $x_c^* = x_B^* = 8.03$. After $x_c^* = x_B^*$ the hydrostatic energy measure, E_0^*, is the most appropriate for this case. The energy then drops momentarily due to the change of energy formula, then remains constant until the wave breaks (x_c^* around 6), after which a strong dissipation ensues.

In this case the dissipation is due to a single shock. The dissipation rate per width, D_{th}, may then be approximated as (Tissier et al., 2011)

$$D_{th}^* = \frac{1}{4}\left(\frac{2h^* + d^*}{2h^*(h^* + d^*)}\right)^{1/2} (d^*)^3, \tag{15}$$

where d^* is the shock height, which, for a fully developed bore, corresponds to maximum η^* (A^*) in our case, and h^* is the undisturbed water depth. The rate D_{th}^* has been made dimensionless by the factor $E_c\sqrt{\frac{g}{h_0}}$, where E_c is given above. In figure 16 we observe that the dissipation rates of the models has a build-up, before the shock is fully developed, and then agree well with formula (15). Moreover, due to larger shock heights the BoussClaw($\epsilon_B = 0.8$) dissipation rate is much larger than that of the NLSW model, when the wave finally has broken. This reduces the difference between the models to some extent.

It is obvious that the NLSW model in this case is severely inaccurate, while it is more difficult to assess the BoussClaw with and without the switch to the NLSW.

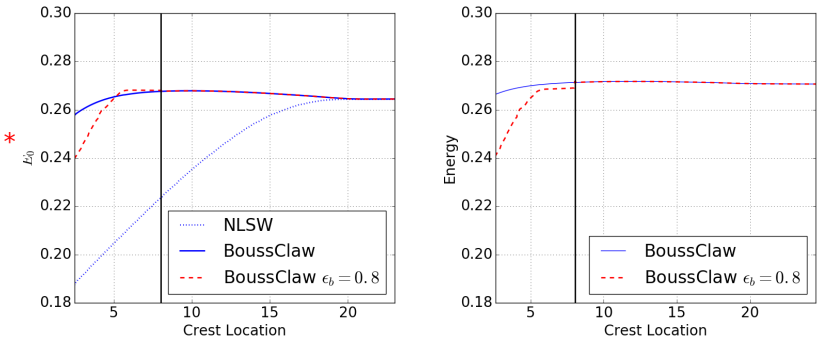

(a) (b)

Figure 15: Wave energy ($\alpha = 0.28$, slope $1 : 19.85$) as function of crest position. The vertical line is at $x^* = 8.03227$ where $\epsilon_B = 0.8$. (a): E_0^*. (b): Solid line is $E_0^* + E_1^*$ of BoussClaw without ϵ_B. With $\epsilon_B = 0.8$, E_0^* is shown in dashed line after the threshold is reached.

Curves stopped before shoreline moves. Or, new energy computations.

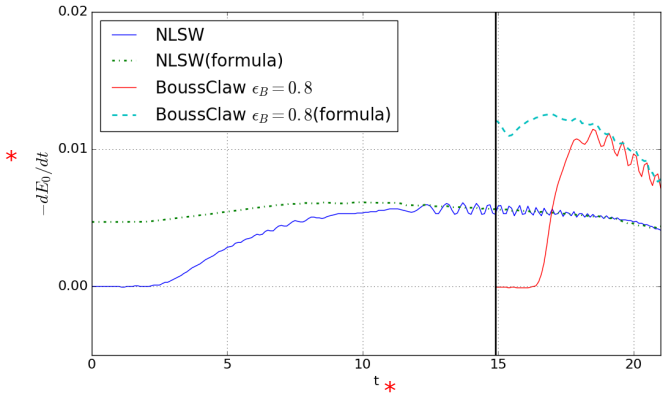

Figure 16: Dimensionless energy dissipation rates for $\alpha = 0.28$ and a $1 : 19.85$ slope. The label "formula" represents (15) inserted the wave heights from the numerical simulations. BoussClaw with $\epsilon_B = 0.8$ switches to the NLSW at $t^* = 14.9$.

The onset of the dissipation in the threshold model comes slightly before the a vertical front is observed in the BIM solution $x_c^* = 4.09$. This may